Three-dimensional virtual histology of the cerebral cortex based on phase-contrast X-ray tomography

MARINA ECKERMANN,[1,2] FRANZISKA VAN DER MEER,[3] PETER CLOETENS,[4] TORBEN RUHWEDEL,[5] WIEBKE MÖBIUS,[2,5] CHRISTINE STADELMANN,[2,3] AND TIM SALDITT[1,2,*]

[1]*Institut für Röntgenphysik, Friedrich-Hund-Platz 1, 37077 Göttingen, Germany*
[2]*Cluster of Excellence "Multiscale Bioimaging: from Molecular Machines to Networks of Excitable Cells" (MBExC), University of Göttingen, Germany*
[3]*Institut für Neuropathologie, Robert-Koch-Straße 40, 37075 Göttingen, Germany*
[4]*ESRF, the European Synchrotron, 71, avenue des Martyrs, 38043 Grenoble Cedex 9, France*
[5]*Max-Planck-Institut für experimentelle Medizin, Hermann-Rein-Straße 3, 37075 Göttingen, Germany*
[*]*tsaldit@gwdg.de*

Abstract: In this work, we optimize the setups and experimental parameters of X-ray phase-contrast computed-tomography for the three-dimensional imaging of the cyto- and myeloarchitecture of cerebral cortex, including both human and murine tissue. We present examples for different optical configurations using state-of-the art synchrotron instruments for holographic tomography, as well as compact laboratory setups for phase-contrast tomography in the direct contrast (edge-enhancement) regime. Apart from unstained and paraffin-embedded tissue, we tested hydrated tissue, as well as heavy metal stained and resin-embedded tissue using two different protocols. Further, we show that the image quality achieved allows to assess the neuropathology of multiple sclerosis in a biopsy sample collected during surgery.

1. Introduction

The human brain is formed by a complex and rapidly interacting network, with information processing within and across specialized subregions [1]. In order to decipher how the brain functions and how function is compromised in different pathological states, structural information is required, covering many length scales. On the macro- and microscale, the cytoarchitecture and myeloarchitecture account for the different types, morphologies, and concentrations of neurons, glial cells and connective fibers, and their connectivity, and is typically assessed by optical microscopy based on histological thin section or cultured tissue slices [2–5]. Optical microscopy in combination with immunohistochemistry constitutes a routine technique of neuropathology and pre-clinical research, for example in neurodegenerative diseases. Small-angle X-ray scattering has also proven to be suitable for studying the myelostructure in murine and human brain tissue [6,7]. On the nanoscale level, neuronal circuits can be probed by modern electron microscopy (EM), in particular serial block face scanning electron microscopy (SBEM) [8,9] or volume-EM by automated transmission-EM (TEM) [10], enabled by advanced heavy metal staining, notably the adapted rOTO-protocols [11–13].

More recently, X-ray phase-contrast computed-tomography (PC-CT) has joined the toolset to study human brain tissue [14–18], as well as small animal models of mammalian brain tissue [19–23]. Similar to conventional CT, PC-CT offers three-dimensional (3d) reconstructions without any need for sectioning, while offering much higher contrast to soft tissues and also resolution, when free-wave propagation is exploited for contrast formation. PC-CT can be implemented both with synchrotron radiation (SR) and compact laboratory sources (μCT). Tissue

volumes can be scanned with adjustable field-of-view and resolution. For larger overviews, parallel-beam (PB) illumination is most efficient, scanning entire biopsy punches within minutes [24] at a resolution limited by the detector pixels size (*i.e.* down to the sub-µm range). Selected subregions can then be probed in cone-beam (CB) geometry down to the sub-100 nm range, below the diffraction limit of optical microscopy. Here, a resolution given by the half-width of the source spot can be achieved, *i.e.* at the level of the focused synchrotron radiation. Applications of PC-CT in human brain sample imaging, in particular of unstained formalin-fixed and paraffin-embedded (FFPE) tissues, have recently been demonstrated. Cellular and sub-cellular structural details can be observed in these preparations [25–27]. Further sample preparation techniques for PC-CT of unstained neuronal tissue exist, including formalin-fixed, dehydrated or hydrated tissue in solution or tissue fixed and embedded in paraffin [20,28–30]. In order to create enhanced contrast for small cellular features and in particular nerve fibers, osmium-based protocols have also been used for PC-CT of tissue from the central nervous system of murine and from the peripheral nervous system both of human and murine tissue [31–34].

Following preceding PC-CT studies on human cerebellum and hippocampus [25,35], the main goal of the current work is to explore to which extent PC-CT could contribute to imaging of the cerebral cortex of the mammalian brain, and in particular of the human brain, which shows a complex neuroanatomy with 10^{15} neuronal connections [1]. We include the corpus callosum (CC), which is the major tract of commissural fibers, with 10^8 nerve filaments connecting both hemispheres of the brain [36]. For the essential neuroscience background, we refer to [1,37]. In this context, we ask to which degree advanced staining protocols can help to increase contrast and resolution. In view of the aforementioned recent progress in heavy metal staining and the preceding advent of SBEM, which has made it possible to address the connectivity problem in small brain volumes [38–40], the question arises whether PC-CT can extend this toolset towards larger brain volumes. If so, it may contribute in future to integrate data from different smaller volumes scanned by SBEM. A recent proof-of-concept demonstrates the potential of PC-CT in this context [41,42]. Here, we investigate which instrumental and optical settings, both at synchrotron and inhouse laboratory sources, can take advantage of different stains: To this end, both conventional-OsO_4 and rOTO staining protocols are applied. At the same time, we further include unstained hydrated, (partially) dehydrated, and FFPE-tissue of the cerebral cortex, as well as OsO_4-stained and epon-embedded sample blocks (cf. Figure 1(d) and Fig. 1(e & f), and supplemental document for experimental concepts of data acquisition).

Figure 1 shows a schematic of the cortical regions, from which tissue autopsies and biopsies are scanned in the present PC-CT study. The sagittal view in Fig. 1(a) shows the CC in cross section, while its frontal view is depicted in (b). Various types of neurons exist throughout the cerebral cortex, detailed in [43]. 80% of the cortical neurons are projection neurons, and they are responsible both for short- and long-range signaling. Figure 1(c) shows a sketch of such a projection neuron, which receives input through its dendrites (top), and processes via its myelinated axon to the axon terminal (bottom). Close to the neuron's dendrites, microglial cells are sketched (µG). µG ensure brain maintenance, and target for example misfolded proteins leading to plaques, or damaged neuronal portions. Astrocytes serve the physical organization of the brain, and together with oligodendrocytes (OD) provide the metabolic supply of synapses. Importantly, ODs wrap axons with concentric myelin sheaths.

Apart from neuroimaging of healthy brain tissue, we also want to focus on the assessment of PC-CT for studies in neurodegenerative diseases. Following our recent PC-CT works on human hippocampal tissue affected by Alzheimer's disease, we here include first scans of human brain tissue biopsies obtained during surgery of a patient suffering from *Multiple Sclerosis* (MS). MS is an inflammatory and neurodegenerative disease, which is pathologically characterized by chronic inflammatory demyelination, accompanied with axonal loss and glial scar formation [44]. Glial scar can occur in any type of brain damage, not restricted to inflammation, and reflects an
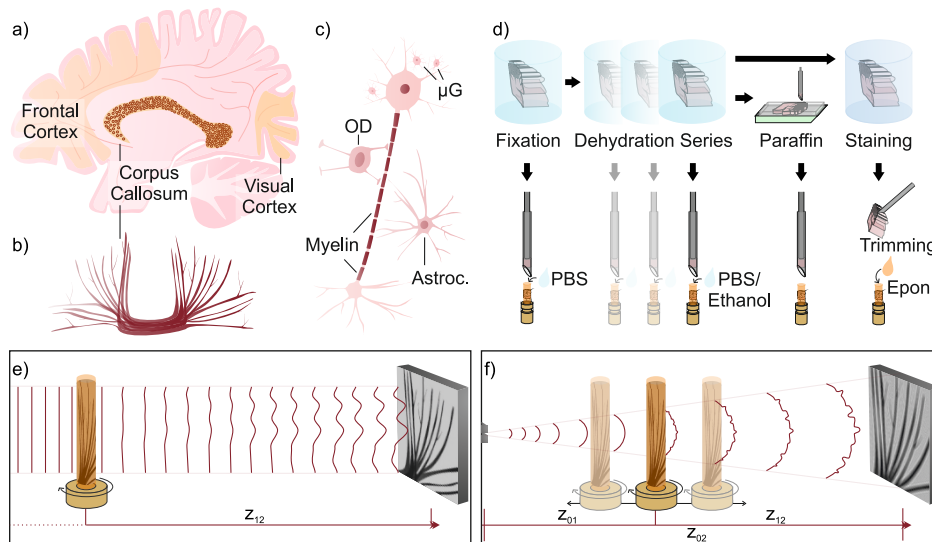
Fig. 1. Basic anatomy, structural features of interest, sample preparation, and measurement principle. (a) Schematic of the human brain in sagittal plane, yellow colors indicate relevant cortical regions for this work: Frontal cortex, visual cortex, and corpus callosum, which is also outlined in coronal plane (b). (c) Schematic of selected cortical structures on a cellular level: neuron with a myelinated axon, microglial cells (μG) in the vicinity of the dendritic tree, oligodendrocytes (OD), and astrocytes (Astroc.). (d) A range of sample preparation protocols are applied, ranging from solely chemical fixation, (partial) dehydration, to (un-)stained solid embedding. PC-CT data are collected (e) in parallel-beam (PB) mode to quickly scan rather large tissue volumes (cf. supplemental document), or (f) exploiting geometrical magnification to zoom into selected regions of interest in cone-beam (CB) geometry (cf. methods in supplemental document). Note that setup-characteristic parameters are indicated: (z_{01}) source-to-sample distance, (z_{02}) source-to-detector distance, and (z_{12}) sample-to-detector distance.

increased number of astrocytes through hyper-proliferation, which rigidifies the tissue. While white matter lesions are rather prominent with clinical routine imaging techniques, pathologies in gray matter emerge unobtrusively. Pathohistological assessment thereof remains a technical challenge [44]. To-date, the insufficient feature contrast is eluded by special myelin protein immunohistochemistry, but also PC-CT could be a potential tool. The astrocyte proliferation is a reaction to stabilize lesions and to keep inflammatory cell from spreading, but at the same time is believed to hinder new neuronal growth [45,46]. Furthermore, astrocytic factors impede the differentiation of OD-progenitor cells. Signs of glial scar formation are completed by increased emergence of μG, resulting in angiogenesis and fibrosis. Damage of the myelin sheath followed by scar formation is also referred to as "MS-plaques". Overall, various forms (chronic, acute) and stages of MS exist [47,48], in which OD even regenerate and remyelinate. According to the definition in [49], normally appearing white matter (WM) refers to tissue with normal axon myelination, without plaques in a radius of $\geq$ 10 mm and no further signs of abnormality, while normally appearing gray matter (GM) shows no signs of demyelination using immunohistochemistry. Normally appearing tissue is distinct from remyelination region, in which shadow plaques (plaques with myelin sheath, "remyelinated lesions") and newly formed myelin sheaths with reduced thickness are found [50]. Here we want to investigate, at which quality structural features can be identified in PC-CT reconstructions.

Next, we briefly introduce the topics of relevance in this work: instrumentation and optics for synchrotron and laboratory PC-CT, sample preparation including unstained, hydrated, and heavy metal stained tissues, and the important role of mouse models, notwithstanding the fact that human brain tissue remains the main incentive of this work.

Laboratory μCT In view of future applications in pathohistology, it is important to assess to which extent phase-contrast imaging of unstained human tissue can be implemented with laboratory μCT. With recent advancements in both reconstruction schemes suitable for low coherence and novel instrumentation, such as transmission-anode X-ray sources with small source spots and sufficient power (for example approx. 300 nm and 0.3 W, respectively, for the N2 NanoTube, Excillum Inc.), partially-coherent illumination can now be implemented at compact laboratory setups for 3d virtual histology analysis [27], even without liquid-jet anode technology which was used in [25,32] or a compact laser-driven synchrotron source [51]. Details on implementations can be found in the supplemental document.

Synchrotron radiation The much higher brilliance and in particular spatial coherence enables focusing to spot sizes in the 10-100 nm range, while preserving high photon flux, now routinely exceeding $>10^9$ ph/s [52–56]. Synchrotron scans in such a cone-beam geometry (SR-CB) with nanometric virtual source offer the highest resolution and potential for further scaling. Due to the correspondingly smaller effective pixel size in the sample plane, data acquisition typically takes place in the so-called deep holographic regime, defined by a very small Fresnel number $F \ll 1$ (cf. supplemental document). Further, using monochromatic illumination, this regime offers highest sensitivity to small phase differences. Consequently, it allows for quantitative interpretation of reconstructed density, based on well-defined optical constants. For recordings in the holographic regime, these are decisive advantages of SR, where single X-ray energies are selected based on multilayer or crystal monochromators, while laboratory PC is always restricted to broad bandpass due to its limited brilliance. Also filtered white or pink SR can be used for PC-CT, offering elevated photon flux. Most SR parallel-beam data (SR-PB) are recorded in the so-called direct contrast regime ($F \leq 1$), which is compatible with broad bandpass. However, for high-resolution studies in the holographic regime, a higher monochromaticity is required. Furthermore, radiation damage can occur more easily for pink beams.

Hydrated and in solution In conventional histopathological analysis, FFPE-sample blocks are prepared by chemical fixation, gradual dehydration and subsequent paraffin infiltration, and further processed through slicing, rehydration, and staining before inspection by optical microscopy. Aside from its 3d capability, virtual histology and pathohistology based on PC-CT can be motivated by the following properties: a different and complementary image contrast based on electron density, compatibility with sample preparations beyond the standard FFPE-scheme, which is known to be associated with pronounced tissue modifications [57–59], and finally the wish to reduce effort and time in sample preparation. To this end, the image quality and performance of PC-CT for liquid-embedded samples has to be further assessed.

Heavy-metal staining Beyond the contrast based on (native) electron density obtained from unstained tissues, feature-specific contrast can be achieved by staining. Osmium tetroxide (OsO_4), for instance, binds to the phospholipid headgroups, and hence gives particular contrast to plasma membranes, multi-vesicular structures, ribosomes and Golgi complexes. Membrane-rich cortical structures such as fiber tracts should therefore emerge particularly. Further to contrast enhancement, chemical fixation of sample tissue is an important property of OsO_4 [60]. Sophisticated classical OsO_4-based protocols exist for EM applications, and have been finetuned for bulk tissue staining, notably as adapted *rOTO* ("reduced osmium, thiocarbohydrazide (TCH), osmium") [12,13], resulting in contrast levels compatible with SBF-SEM connectomic studies [8,9]. Reducing agents, such as potassium ferrocyanide, are one key aspect of rOTO, converting Os^{VIII} to reduced oxidation states [11]. As a result, larger amounts of osmium are deposited onto the membrane. However, in conventional rOTO [61], the penetration depth typically does not

exceed 200 µm. In order to overcome this limitation, the reducing agent can be applied only right after deep osmium penetration. Consequently, this rOTO modification [11] can surmount staining rings at the tissue periphery and limited penetration depth, making it possible to process mm-thick tissue blocks. While this is well-established for EM, for PC-CT, osmium-based staining gave good results for tissue of the peripheral nervous system [31,62–63], and, to some extent, of the central nervous system [29,34,64–66]. However, staining protocols specifically optimized for PC-CT, *i.e.* in view of volume suitability and contrast agent density, are still lacking. Recently, well-established procedures from conventional histology have been adapted for PC-CT [67,68]. Regarding heavy metal protocols from EM, it is less clear how heavy metals are the most suitable approach for PC-CT. There are still many open questions regarding the most suitable protocols for given tissue type, photon energy, instrumentation (SR versus laboratory µCT) and phase retrieval approach. First findings demonstrate that the modified rOTO protocol from [11] is also well suited for SR-PC [42]. Still, to-date, PC-CT applications using heavy metal stains for tissue of the central nervous system have been reported only for small animal models, and not for human tissue.

Murine brain tissue The mouse brain is an indispensable example for the neurobiology of the mammalian brain in order to unravel mechanisms of different neurodegenerative diseases in genetically well-controlled mutants. As far as imaging is concerned, small animal models offer some advantages in tissue preparations as compared to human tissues. Optimized fixation, such as perfusion of the mouse brain and more control of the preparation protocol, can be expected to result in better preservation of the tissue's ultrastructure [69]. At the same time, neurons of the mouse brain are smaller and of lower (native) electron density, compared to human, which can pose a greater challenge for PC-CT, see for example the image quality of human [25] and murine cerebellum [20] for recordings of similar experimental settings. Furthermore, studies of murine brain tissue are adequate to develop and refine sample preparation protocols, which can later be partially translated to human tissue, under the constraints given by clinical pathology.

At the end of this introduction, we briefly outline the further organization of this manuscript. In the following results section, we first address unstained human brain tissue, comparing paraffin-embedded and hydrated samples, as well as results obtained with synchrotron radiation (SR) and laboratory instrumentation (µCT), before we focus on heavy metal stains both in human and murine cortical tissue. We close with a discussion section presenting the main conclusions and an application outlook.

2. Results

First, we turn to PC-CT results obtained for unstained tissue of the human cortex, comparing formalin-fixed, dehydrated and paraffin-embedded (FFPE) with hydrated samples, as well as synchrotron radiation (SR) and compact laboratory sources (µCT). The image quality and volume information in each image configuration can be assessed in view of future applications for histopathological inspection and analysis. For these and all further datasets, details on sample preparation and experimental setups are given in the supplemental document, with data acquisition and reconstruction settings listed in Tab. S1-S3.

Figure 2 presents an overview over PC-CT reconstructions and segmentation of neurons from parallel and cone-beam synchrotron radiation (SR1-PB and SR1-CB configuration, cf. supplemental document). All samples are unstained and embedded in paraffin, collected as 1 mm biopsy punches from FFPE-tissue blocks. While all panels indicated by (a) refer to tissue collected during *post mortem* routine autopsy from a (neuropathologically) normal subject, panels indicated by (b & c) refer to biopsy tissues samples from a patient diagnosed with MS, and collected during surgery. Notably, sample (c) has been extracted from a region of normal appearing gray matter, and (b) from a remyelinated region of an individual with MS, as defined in the introduction. With regard to the feature pathology in the remyelinated region, the normally appearing sample can be
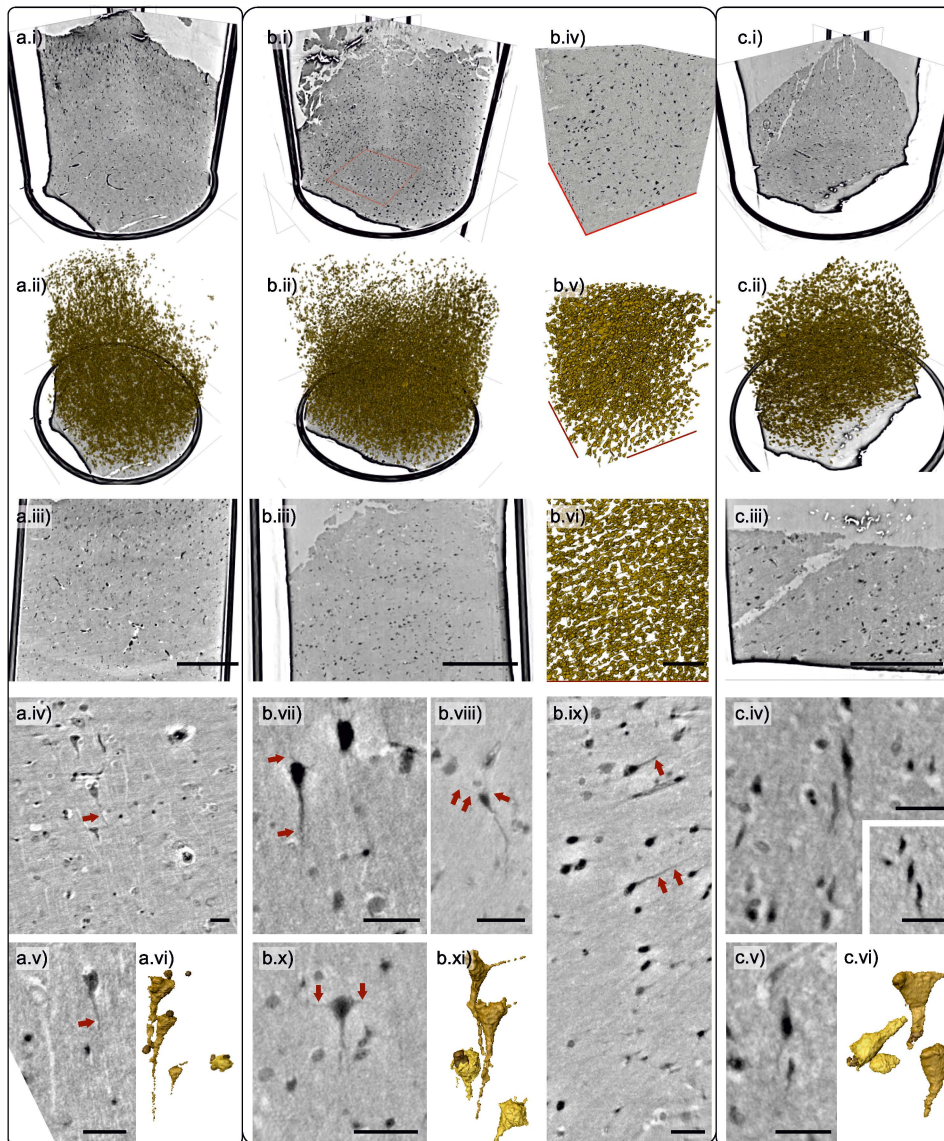
Fig. 2. Human cortical tissue, unstained FFPE-preparation, SR1 scans. (a) cortex control tissue sample, collected *post mortem*, (b & c) cortex tissue samples collected from a subject diagnosed with Multiple Sclerosis (MS) during surgery: (b) from a remyelination region, (c) from normally appearing cortex. Top three rows show slices and volume renderings of neurons from SR1 data: (a.i-iii,b.i-iii,c.i-iii) present reconstructions from SR1-PB scans, (otherwise) higher resolution reconstruction from a SR1-CB scan of the region marked in (b.i). Fiber structures and neurons with delicate dendrites (exemplary highlighted by arrows), and associated cells are depicted as single slices or Maximum Intensity Projections (MIPs), with projection thickness given by: (a.iv & v, c.iv-inset) 2 μm, (b.vii & ix) 1 μm, (c.v) 1.6 μm. (a.vi, b.xi, c.vi) Volume renderings of four representative neurons and microglia. Scale bars: (a.iii, b.iii, c.iii) 300 μm, (b.vi) 100 μm, (otherwise) 30 μm.

considered as a control presenting the same subject-specific and tissue processing conditions, while (a) represents a control in a wider-range pathological sense. Figure 2(a-c.i) shows overview

orthoslices from the 1 mm biopsy punches, recorded in SR1-PB configuration, with (a-c.ii) showing corresponding volume renderings of neuronal structures, and (a-c.iii) planar slices. For the remyelinated sample, (b.iv) shows a region-of-interest (ROI) corresponding to the marked region in (b.i), which has subsequently been scanned in SR1-CB configuration. (b.v & vi) present volume renderings of the ROI, with neuron shapes and axons showing a strong orientation. In the two lower rows, single neurons are highlighted, recorded in SR1-CB configuration for all three samples. In each data set, neurons with both a particularly high and low electron density can be found. Axonal fibers are well-contrasted based on their native electron density, and even the dendrites can be distinguished in some cases. Further, for the control sample data shown in (a.iv), the spatially oriented fibers emerge with a lower electron density (lighter color) compared to the surrounding tissue, as opposed to the biopsy samples. In all three samples, the image quality and resolution is sufficient for gray-value based segmentation, as illustrated by selected segmentations of neurons along with smaller bordering cells, which can tentatively be identified as microglias. The corresponding renderings (a.vi,b.xi,c.vi) were all obtained manually using Avizo Lite (Thermo Fisher Sci.).

As discussed in the introduction, it is of interest to explore to which extent PC-CT can be applied to unstained tissue beyond the standard FFPE-scheme, which can suffer from dehydration artifacts, and for which more preparation steps are required compared to simple fixation and embedding of tissue in buffer or solvent. Here we examine the image quality and performance of
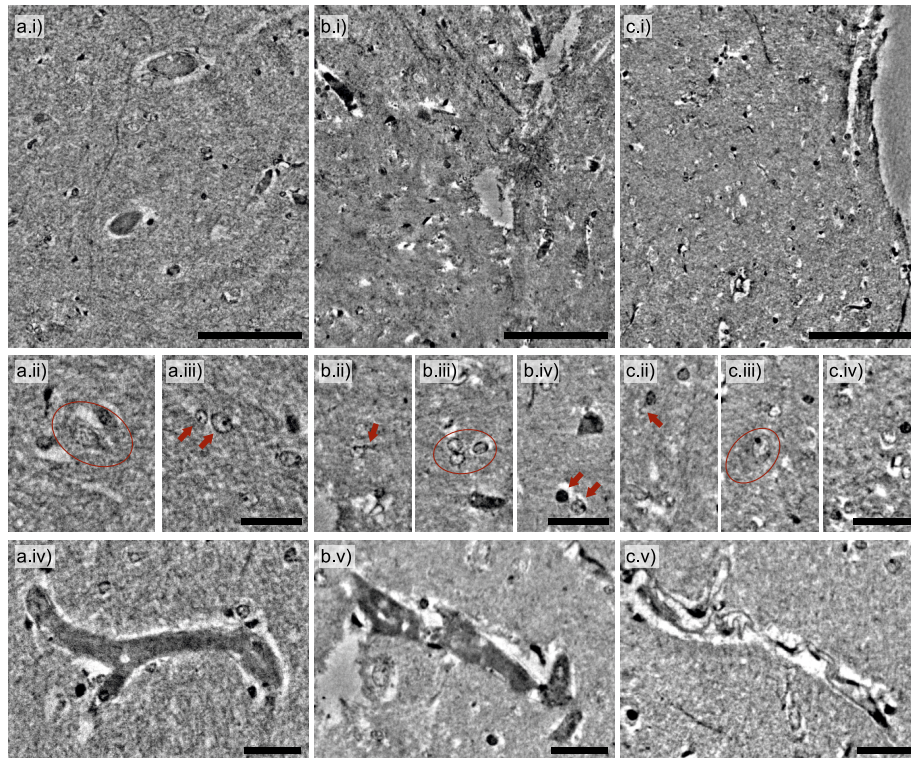

Fig. 3. Human cortical tissue, unstained in liquid, SR1 scans: (a) Fully hydrated in PBS (0% dehydration), (b) in 30% PBS 70% ethanol, and (c) in 100% ethanol. (Top row) Depiction of the overall tissue structure, (middle row) selected regions highlighting single cells and dendritic structures, (bottom row) vasculature changing appearance during dehydration. Scale bars: (a-c.i) 100 μm, (otherwise) 30 μm.

PC-CT for liquid-embedded human cortical tissue, following up our previous work on cerebellum [20]. To this end, Fig. 3 presents results obtained for cortical tissue of a single human (control), scanned in SR1-CB configuration in three different liquids, representing a *dehydration series*: (a) fully hydrated in PBS (0% dehydration), (b) 30% PBS 70% ethanol, and finally (c) in 100% ethanol. Overview slices in (a-c.i) show reasonable tissue contrast for all steps of preparation. Figure 3 (middle row) features single cells: cell bodies, nuclei and nucleoli can be clearly distinguished, and even also cellular dendrites. Inspection of the data gives an impression of cellular shrinkage with increasing ethanol infiltration. Overall tissue volume reduction from dehydration is well-known. However, the observation also depends on the exact cellular type. For example, cells marked in (a.ii) and (c.iii) both emerge particularly strong and with similar size despite the different solvents. In Fig. 3 (lower row), the pronounced impact of dehydration on vessel architecture stands out.

Next, we assess to which extent phase-contrast of unstained human tissue can be exploited in laboratory μCT (cf. supplemental document).Figure 4 demonstrates that this approach can indeed yield convincing image quality for unstained human cortical tissue, with sufficient contrast for neurons and axons. Note that this example is presented for the biopsy samples collected during surgery, pointing out the potential for future use of PC-CT in clinical pathological diagnostics. Both setups yield very similar feature visibility and comparatively high resolution, owing to the sub-μm spot size of both sources, but differ in the detector technology, *i.e.* indirect fibre-coupled CCD (μCT1) versus direct detection with a single-photon counting pixel detector (μCT2). This
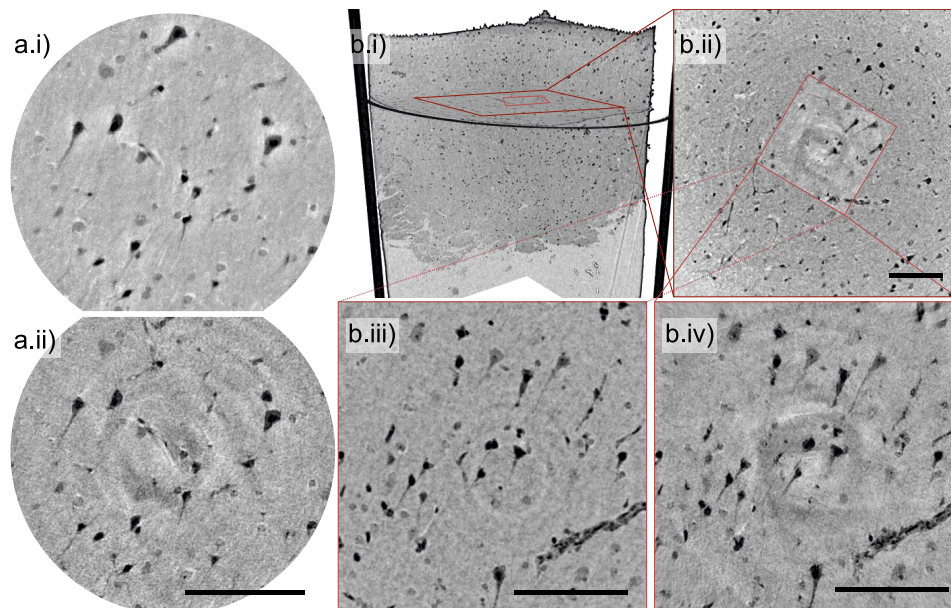

Fig. 4. Human cortical biopsies, unstained FFPE-preparation, laboratory-based PC-CT. Reconstructions are shown for a tissue biopsy collected during surgery from the remyelinated region of a subject diagnosed with MS. (a) Comparison between SR and laboratory: reconstruction of the same regions from (a.i) SR1-CB data, and (a.ii) L2-data, both represented as Maximum Intensity Projections (MIPs) over 1.4 μm thickness. (b) Overview scans and ROIs, reconstructed from (b.i & ii) μCT1 data. Squares mark regions recorded with 350 nm voxel size, using μCT2, pasted into the μCT1 reconstruction as an inset. (b.iii & iv) MIPs with 6 μm thickness of the same region, scanned with μCT1 & μCT2, respectively. Scale bars: (b.ii) 140 μm, (otherwise) 100 μm.

also accounts for the observed differences in the ring artifacts, observed in µCT2 data, which can be attributed to the inter-module gaps of the single-photon counting detector.

We move from unstained tissue, *i.e.* PC-CT with contrast based on (native) electron density, to contrast-enhancement from heavy metal staining. Previous PC-CT studies of the central nervous system using heavy metal stains have been reported only for small animal models, and not for human tissue. In Fig. 5, the conventional OsO_4-staining procedure (cf. supplemental document) has been applied to human *post mortem* tissue, notably (a) gray and (b) white matter (GM, WM). (a.i & ii) show volume renderings of myelinated structures and corresponding virtual sections. By adjusting geometric magnification and source size, the tissue was scanned at 350 nm voxel size, see (a.iii-iv) for examples with µCT1. A tool developed for segmentation of single myelinated axons in synchrotron nanotomography data [62] was also applied here for a proof-of-concept that fiber tracing can be performed at the level of quality achievable from laboratory PC-CT of stained tissue, see the rendering in (a.iv). OsO_4-stained human WM is shown in Fig. 5(b), for data from (b.i) µCT2 (0.99 µm voxels), and from (b.iv-v) SR1-PB, and in more detail for (b.ii-iii) data obtained at µCT2 (0.65 µm voxels) and (b.vi-viii) SR1-CB. Even in rather large FOV-scans, the delicate myelinated fibers which are on the order of a few microns in width can be identified based on the contrast provided by the conventional OsO_4-stain. Note that in (b.vii & viii), the source-to-sample-distance has been decreased, affecting the geometric magnification of single resolution elements from 159 nm to 49 nm.

After having presented examples of human tissue above, we now turn to PC-CT of small animal models, more explicitly murine tissue of the central nervous system. In particular, we present PC-CT results of murine brain tissue for the conventional-OsO_4 protocol, and the rOTO-technique, both applied to K&S-fixed murine cortical tissue (cf. supplemental document). As expected, the heavy metal staining helps to extend the application range of laboratory µCT. Fig. 6 shows reconstructions from laboratory µCT1-data, for (a) rOTO- and (b) conventional-OsO_4 staining.

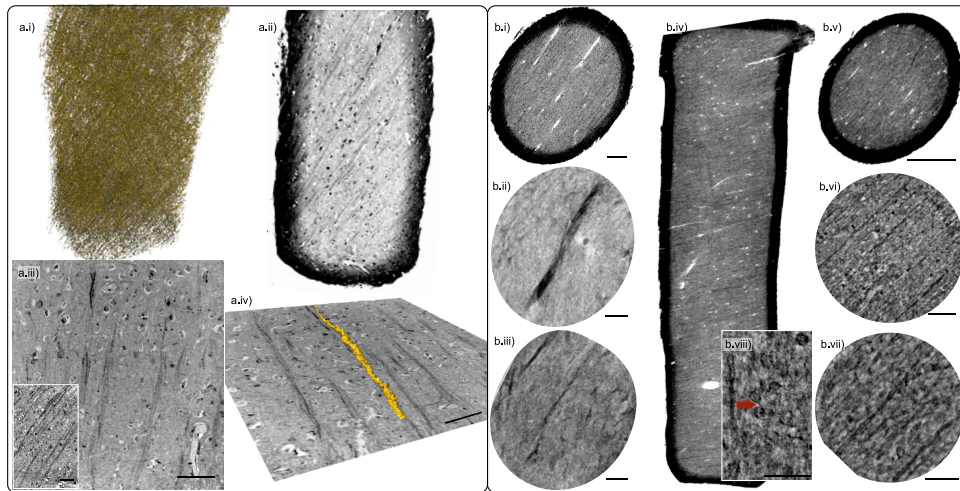**Fig. 5.** Human cortical tissue, OsO_4-stained, SR1-PB, SR1-CB, µCT2. The examples show *post mortem* human cortical tissues from: (a) GM and (b) WM. After overview scans recorded at (a.i-ii & b.i) the µCT1, (b.ii-iii) the µCT2, and (b.iv-v) the SR1-PB setup, more detailed scans were recorded with (a.iii-iv) µCT1 and (b.vi-viii) SR1-CB configuration. (a.i) Volume rendering of stained fibrous structures within the entire punch. In (a.iv), a neuron was tracked and segmented based on its contrasted myelin sheath. MIPs over (b.i) 11.5 µm, (b.v) 2 µm, (b.vii) 0.35 µm, (b.viii) 0.5 µm thickness. Scale bars: (b.v) 300 µm, (b.vi-viii) 50 µm, (otherwise) 100 µm.
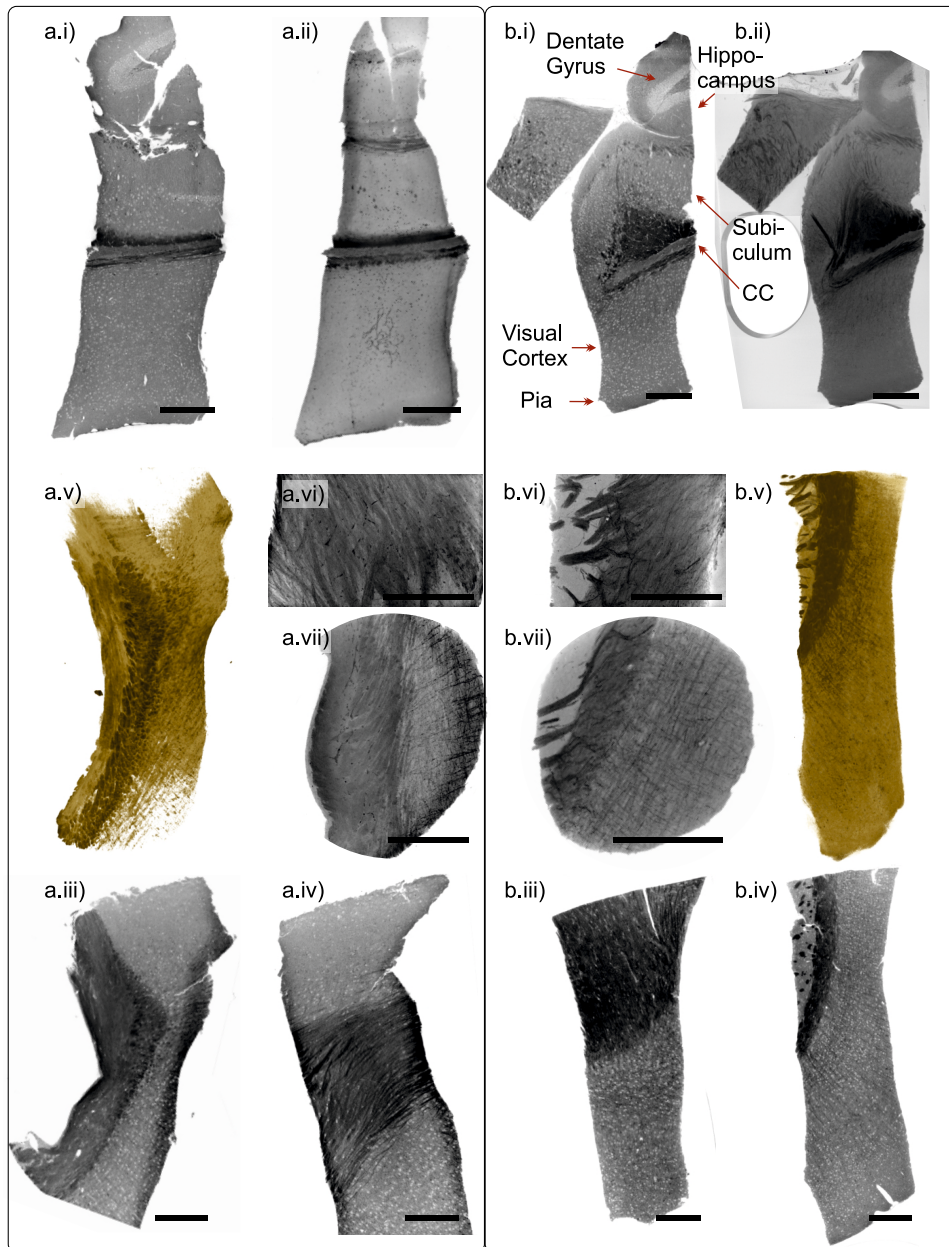
Fig. 6. Murine brain tissue, different heavy metal stains, laboratory CT. Virtual sections, MIPs and volume renderings are shown for (a) rOTO-protocol, and (b) conventional OsO_4-staining. (a.ii & b.ii) MIP over 100 μm, (a.vi) MIP 20 over μm, and (a.vii, b.vi & vii) MIP over 35 μm thickness. (a.v & b.v) volume renderings, (otherwise) virtual sections. Scale bars: 300 μm.

The samples depicted in (a.i-b.ii) have been extracted along the craniocaudal axis, and comprise a number of different brain regions. With the CC as the most massive part of the commissural fibers, it emerges particularly contrasted. This region is further depicted in Fig. 6 (middle & bottom row), with (a.iii-b.iv) showing virtual sections, and (a & b.v) reconstructed volumes
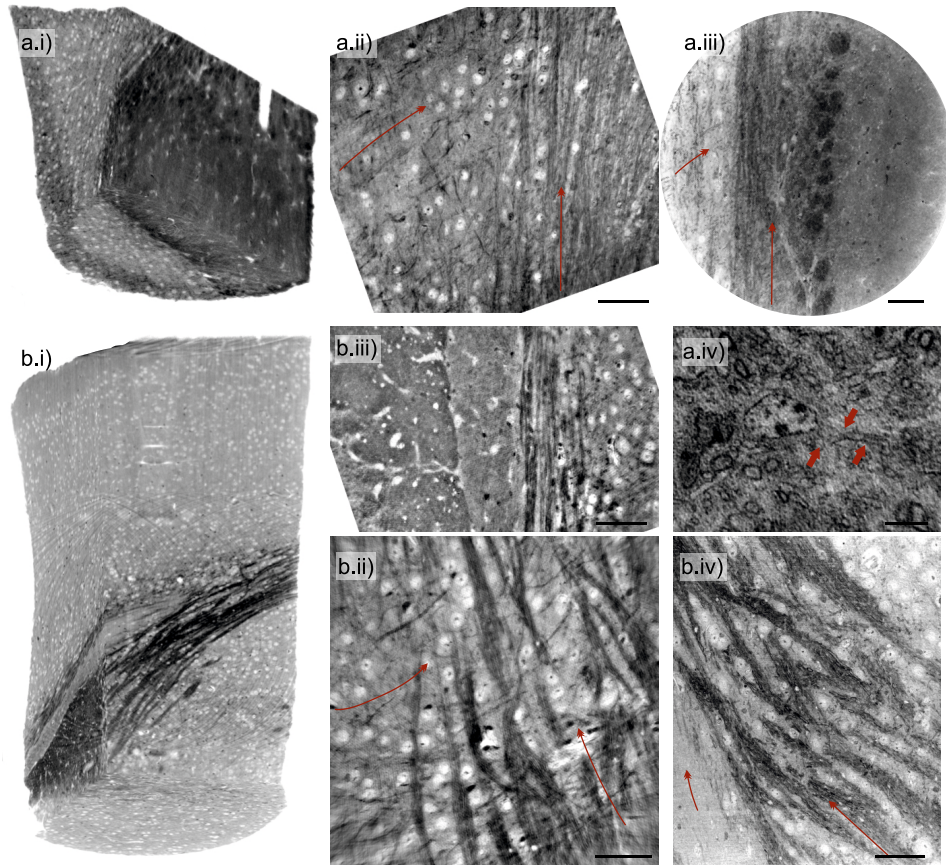
Fig. 7. Murine corpus callosum (CC), stained with the (a) rOTO protocol and (b) conventional-OsO$_4$ (cf. supplemental document), using (a.i & b.i) the SR1-PB, (a.ii & b.ii-iii) SR1-CB and (a.iii-iv & b.iv) SR2. Elongated arrows indicate the general fiber orientation, accentuating the cross-fiber organization of the CC, and bold arrows mark cell body membrane with axonal extensions. Scale bars: (a.iv) 5 μm, (otherwise) 50 μm.

rendered purely based on the voxel gray-values. With high-resolution settings for setup μCT1, inter-layer connections are studied locally in (a.vi-b.vii).

Heavy-metal stains can also help to increase resolution and image contrast in synchrotron PC-CT. Figure 7 presents an overview of SR1-PB (parallel-beam) and SR1-CB (cone-beam configuration) data obtained on the same murine samples as in Fig. 6, again labeled (a) for rOTO-protocol and (b) for conventional OsO$_4$-staining. Panels (a-b.i) have been acquired with the SR1-PB setting. The fibroid nature of the CC is very clearly represented already on larger scale for rOTO. Neuronal cell bodies emerge with lighter contrast in both protocols. In (a.ii & b.ii-iii) and (a.iii-iv & b.iv) higher resolution scans are presented, acquired in the SR1-CB and SR2 setup, respectively. In these reconstructions, the cylindrical myelin sheath around the axons is clearly resolved and single axons can be traced in 3d. Not all myelinated fibers in the CC are oriented along the same direction, as exemplary indicated by the elongated arrows. In the scans shown in (a.iv), the voxel size was further reduced from 130 nm to 50 nm. The myelinated axon shapes are well-resolved and contrasted. They are recognized in longitudinal section, and in cross-sectional view, as marked by arrows. Further, pronounced variations in electron density are
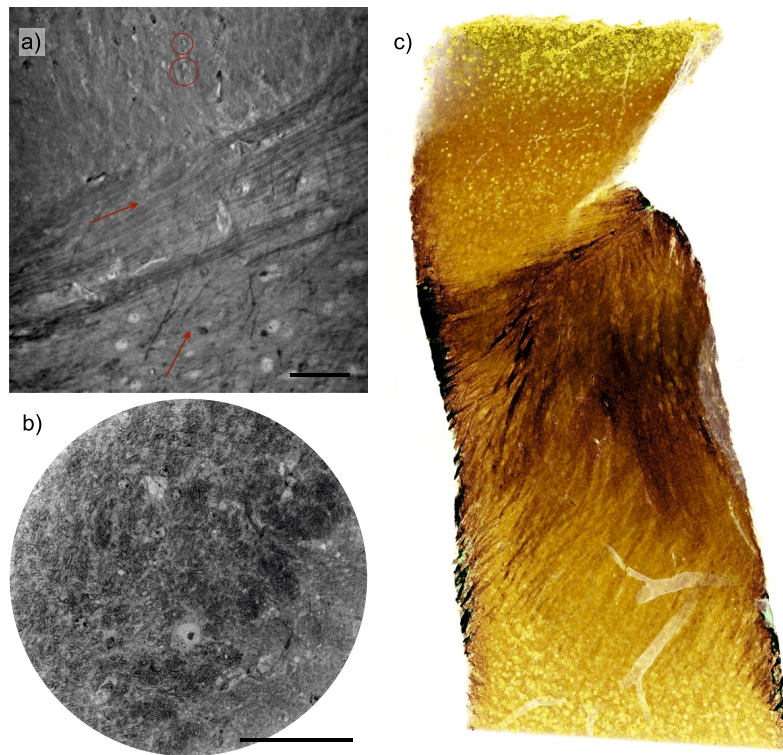
Fig. 8. Murine CC, rOTO-stained, recorded with (a) SR1-CB, (b) SR2 and (c) μCT1. Arrows indicate general fiber orientation in the section, emphasizing the organization of the CC, and circles exemplary highlight single neurons. Scale bars: 50 μm.

resolved in the nucleus, indicative of heterochromatin. Again, the exact settings of all scans are listed in Tab. S1 & S2.

Finally, Fig. 8 closes the presentation by highlighting the results obtained for the rOTO-stain at high magnification, both with synchrotron radiation (SR1-CB, SR2), and high resolution laboratory (μCT1). Panels (a) and (b) show two virtual sections of rOTO-stained murine CC tissue, while (c) presents a rendering of a μCT1 laboratory dataset (visualization with NVIDIA IndeX). The wealth of neural cell bodies and the complex fiber structures in the CC, jointly with negatively contrasted vasculature, emerge particularly in this presentation.

3. Discussion

In summary, the examples presented above demonstrate the capability of PC-CT to cover mm^3-sized tissue volumes with convincing image details regarding the neuronal cyto- and myeloarchitecture. Different imaging demands require different field-of-view, voxel size and resolution, as well as contrast. In most general terms, this can be met by adaptation of the tissue preparation, staining, choice of photon energy and flux, the instrumental and geometric settings, and reconstruction algorithms. The present work gives some examples how settings and parameters can hence be tuned and shifted accordingly. We draw the following conclusions:

- Following previous PC-CT of human cerebellum and hippocampus, the present work demonstrates that the technique is well-suited to address also the highly-structured and interconnected cytoarchitecture of human cerebral cortex, see Fig. 2–5.

- Beyond *post mortem* autopsies, biopsies of human brain tissue collected during surgery can be scanned for histopathological assessment, see Fig. 4.

- Hydrated neuronal tissue can be reconstructed with considerable image quality, see Fig. 3. Liquid embedding requires the SR1 setting, and is currently incompatible with vacuum settings such as in SR2.

- The higher photon energy of 17.1 keV possible at SR2 in combination with elevated photon flux of $2 \cdot 10^{11}$ ph/s allows for very convincing scans of neuronal tissue stained according to the rOTO protocol. Rather than SR1, these properties allow for more reasonable cross sections in the range of 300-400 μm.

- Staining can augment laboratory μCT to the sub-μm range.

- The instrumental stability and unprecedented high flux in KB nanofocus results in less noise and higher resolution for SR2 compared to SR1, see for example the highly resolved neuronal nuclei in Fig. 7(a.iv).

- The high coherence (longitudinal and spatial due to WG filtering) at SR1 enables reconstruction at favorable dose-to-resolution ratios, and is particularly well-suited for unstained tissue, also based on its lower photon energy. Dose estimates are given in Tab. S2.

- A major asset of SR, apart from much smaller scan times and higher throughput, is monochromaticity, and the resulting quantitative contrast based on meeting the assumptions of phase retrieval algorithms [14].

- At the same time, laboratory μCT becomes quite competitive for larger scan volumes and stained specimen, as in Fig. 6, since the broad bandpass enables a versatile image contrast, with contributions both from phase and absorption.

- The full potential of SR for PC-CT of neuronal tissue could best be exploited by combining the full-field CT acquisition with further stitching protocols. The goal to increase the volume up to three orders of magnitude seems not unrealistic, if dose-induced sample degradation and local tomography errors could be mitigated, e.g. by advanced local tomography algorithms [70].

- Shifting the measurement window in the other direction, the resolution of SR-CB recordings should be further scaled up, for example by the super-resolution holography approach and pixel detectors [53].

Concerning applications, we note down the following reflections:

- For neuropathology and pre-clinical research, in particular on neurodegenerative diseases, unstained FFPE- or solvent-embedded tissue is suitable, and the laboratory CT can be a valuable tool.

- For research in neuroscience, and in particular for addressing the connectivity problem, PC-CT requires high-magnification and high-resolution SR-CB settings, and has to be further scaled up in performance. The challenge is to achieve higher resolution and contrast to identify synapses while maintaining a field-of-view which offers an advantage with respect to EM.

- For the current datasets at high resolution, synapses should be visible, but the identification would require guidance and validations by correlative imaging, in particular by EM. Datasets of the current work will be made available upon request for independent inspection.

Note that all of the above statements have to be taken with a grain of salt. They also reflect the choices and preferences of the authors in view for future work and directions, based on the presented results. Of course, we expect that other valuable perspectives and ideas will be expressed in the field, and that technical progress in optics, instrumentation, reconstruction algorithms and finally sample preparation will provide further progress in the near future.

Disclosures. The authors declare no conflicts of interest.

Data availability. Data underlying the results presented in this paper are not publicly available at this time but may be obtained from the authors upon request. ESRF data (SR2 setup) will become public in 2024.

Supplemental document. See Supplement 1 for supporting content.

References

1. O. Sporns and J. D. Zwi, "The small world of the cerebral cortex," Neuroinformatics **2**(2), 145–162 (2004).
2. J. Kim, T. Zhao, R. S. Petralia, Y. Yu, H. Peng, E. Myers, and J. C. Magee, "mGRASP enables mapping mammalian synaptic connectivity with light microscopy," Nat. Methods **9**(1), 96–102 (2012).
3. S.-Y. Kim, K. Chung, and K. Deisseroth, "Light microscopy mapping of connections in the intact brain," Trends Cognit. Sci. **17**(12), 596–599 (2013).
4. L. J. Nicolaï, A. Ramaekers, T. Raemaekers, A. Drozdzecki, A. S. Mauss, J. Yan, M. Landgraf, W. Annaert, and B. A. Hassan, "Genetically encoded dendritic marker sheds light on neuronal connectivity in drosophila," Proc. Natl. Acad. Sci. **107**(47), 20553–20558 (2010).
5. F. Y. Shen, M. M. Harrington, L. A. Walker, H. P. J. Cheng, E. S. Boyden, and D. Cai, "Light microscopy based approach for mapping connectivity with molecular specificity," Nat. Commun. **11**(1), 4632 (2020).
6. T. H. Jensen, M. Bech, O. Bunk, A. Menzel, A. Bouchet, G. Le Duc, R. Feidenhans, and F. Pfeiffer, "Molecular x-ray computed tomography of myelin in a rat brain," NeuroImage **57**(1), 124–129 (2011).
7. K. Joppe, J.-D. Nicolas, T. A. Grünewald, M. Eckermann, T. Salditt, and P. Lingor, "Elemental quantification and analysis of structural abnormalities in neurons from Parkinson's-diseased brains by x-ray fluorescence microscopy and diffraction," Biomed. Opt. Express **11**(7), 3423–3443 (2020).
8. M. Helmstaedter, K. L. Briggman, S. C. Turaga, V. Jain, H. S. Seung, and W. Denk, "Connectomic reconstruction of the inner plexiform layer in the mouse retina," Nature **500**(7461), 168–174 (2013).
9. M. Helmstaedter, "Cellular-resolution connectomics: challenges of dense neural circuit reconstruction," Nat. Methods **10**(6), 501–507 (2013).
10. J. S. Phelps, D. G. C. Hildebrand, B. J. Graham, A. T. Kuan, L. A. Thomas, T. M. Nguyen, J. Buhmann, A. W. Azevedo, S. Sustar, A. Agrawal, M. Liu, B. L. L.Shanny, J. Funke, J. C. Tuthill, and W.-C. A. Lee, "Reconstruction of motor control circuits in adult drosophila using automated transmission electron microscopy," Cell **184**(3), 759–774.e18 (2021).
11. Y. Hua, P. Laserstein, and M. Helmstaedter, "Large-volume en-bloc staining for electron microscopy-based connectomics," Nat. Commun. **6**(1), 7923 (2015).
12. S. Mikula, J. Binding, and W. Denk, "Staining and embedding the whole mouse brain for electron microscopy," Nat. Methods **9**(12), 1198–1201 (2012).
13. S. Mikula and W. Denk, "High-resolution whole-brain staining for electron microscopic circuit reconstruction," Nat. Methods **12**(6), 541–546 (2015).
14. A.-L. Robisch, M. Eckermann, M. Töpperwien, F. van der Meer, C. Stadelmann-Nessler, and T. Salditt, "Nanoscale x-ray holotomography of human brain tissue with phase retrieval based on multienergy recordings," J. Med. Imaging **7**(1), 013501 (2020).
15. C. Bikis, G. Rodgers, H. Deyhle, P. Thalmann, A. Hipp, F. Beckmann, T. Weitkamp, S. Theocharis, C. Rau, G. Schulz, and B. Müller, "Sensitivity comparison of absorption and grating-based phase tomography of paraffin-embedded human brain tissue," Appl. Phys. Lett. **114**(8), 083702 (2019).
16. C. Walsh, P. Tafforeau, W. L. Wagner, D. J. Jafree, A. Bellier, C. Werlein, M. P. Kühnel, E. Boller, S. Walker-Samuel, J. L. Robertus, D. Long, J. Jacob, S. Marussi, E. Brown, N. Holroyd, D. Jonigk, M. Ackermann, and P. Lee, "Multiscale three-dimensional imaging of intact human organs down to the cellular scale using hierarchical phase-contrast tomography," bioRxiv (2021).
17. T. Donath, F. Pfeiffer, O. Bunk, C. Grünzweig, E. Hempel, S. Popescu, P. Vock, and C. David, "Toward clinical x-ray phase-contrast ct: demonstration of enhanced soft-tissue contrast in human specimen," Invest. Radiol. **45**(7), 445–452 (2010).

18. R. Gradl, M. Dierolf, B. Günther, L. Hehn, W. Möller, D. Kutschke, L. Yang, M. Donnelley, R. Murrie, A. Erl, T. Stoeger, B. Gleich, K. Achterhold, O. Schmid, F. Pfeiffer, and K. S. Morgan, "In vivo dynamic phase-contrast x-ray imaging using a compact light source," Sci. Rep. **8**(1), 6788 (2018).

19. M. Töpperwien, M. Krenkel, D. Vincenz, F. Stöber, A. M. Oelschlegel, J. Goldschmidt, and T. Salditt, "Three-dimensional mouse brain cytoarchitecture revealed by laboratory-based x-ray phase-contrast tomography," Sci. Rep. **7**(1), 42847 (2017).

20. M. Töpperwien, A. Markus, F. Alves, and T. Salditt, "Contrast enhancement for visualizing neuronal cytoarchitecture by propagation-based x-ray phase-contrast tomography," NeuroImage **199**, 70–80 (2019).

21. M. Hoshino, K. Uesugi, T. Tsukube, and N. Yagi, "Quantitative and dynamic measurements of biological fresh samples with x-ray phase contrast tomography," J. Synchrotron Radiat. **21**(6), 1347–1357 (2014).

22. M. Viermetz, L. Birnbacher, M. Willner, K. Achterhold, F. Pfeiffer, and J. Herzen, "High resolution laboratory grating-based x-ray phase-contrast ct," Sci. Rep. **8**(1), 15884 (2018).

23. L. C. Croton, K. S. Morgan, D. M. Paganin, L. T. Kerr, M. J. Wallace, K. J. Crossley, S. L. Miller, N. Yagi, K. Uesugi, S. B. Hooper, and M. J. Kitchen, "In situ phase contrast x-ray brain ct," Sci. Rep. **8**(1), 11412 (2018).

24. J. Frohn, D. Pinkert-Leetsch, J. Missbach-Güntner, M. Reichardt, M. Osterhoff, F. Alves, and T. Salditt, "3d virtual histology of human pancreatic tissue by multiscale phase-contrast x-ray tomography," J. Synchrotron Radiat. **27**(6), 1707–1719 (2020).

25. M. Töpperwien, F. Van der Meer, C. Stadelmann, and T. Salditt, "Three-dimensional virtual histology of human cerebellum by X-ray phase-contrast tomography," Proc. Natl. Acad. Sci. **115**(27), 6940–6945 (2018).

26. A. Khimchenko, C. Bikis, A. Pacureanu, S. E. Hieber, P. Thalmann, H. Deyhle, G. Schweighauser, J. Hench, S. Frank, M. Müller-Gerbl, G. Schulz, P. Cloetens, and B. Müller, "Hard X-ray nanoholotomography: large-scale, label-free, 3D neuroimaging beyond optical limit," Adv. Sci. **5**(6), 1700694 (2018).

27. M. Eckermann, M. Töpperwien, A.-L. Robisch, F. van der Meer, C. Stadelmann, and T. Salditt, "Phase-contrast x-ray tomography of neuronal tissue at laboratory sources with submicron resolution," J. Med. Imaging **7**(1), 013502 (2020).

28. G. Schulz, A. Morel, M. S. Imholz, H. Deyhle, T. Weitkamp, I. Zanette, F. Pfeiffer, C. David, M. Müller-Gerbl, and B. Müller, "Evaluating the microstructure of human brain tissues using synchrotron radiation-based micro-computed tomography," Proc. SPIE **7804**, 78040F (2010).

29. G. E. Barbone, A. Bravin, A. Mittone, M. J. Kraiger, M. H. de Angelis, M. Bossi, E. Ballarini, V. Rodriguez-Menendez, C. Ceresa, G. Cavaletti, and P. Coan, "Establishing sample-preparation protocols for x-ray phase-contrast ct of rodent spinal cords: aldehyde fixations and osmium impregnation," J. Neurosci. Methods **339**, 108744 (2020).

30. G. E. Barbone, A. Bravin, A. Mittone, S. Grosu, J. Ricke, G. Cavaletti, V. Djonov, and P. Coan, "High-spatial-resolution three-dimensional imaging of human spinal cord and column anatomy with postmortem x-ray phase-contrast micro-CT," Radiology **298**(1), 135–146 (2021).

31. M. Bartels, M. Krenkel, P. Cloetens, W. Möbius, and T. Salditt, "Myelinated mouse nerves studied by x-ray phase contrast zoom tomography," J. Struct. Biol. **192**(3), 561–568 (2015).

32. M. Töpperwien, M. Krenkel, F. Quade, and T. Salditt, "Laboratory-based x-ray phase-contrast tomography enables 3D virtual histology," Proc. SPIE **9964**, 99640I (2016).

33. M. Töpperwien, M. Krenkel, T. Ruhwedel, W. Möbius, A. Pacureanu, P. Cloetens, and T. Salditt, "Phase-contrast tomography of sciatic nerves: image quality and experimental parameters," J. Phys.: Conf. Ser. **849**(1), 012001 (2017).

34. M. Eckermann, M. Töpperwien, T. Ruhwedel, W. Möbius, and T. Salditt, "Evaluation of different heavy-metal stains and embedding media for phase contrast tomography of neuronal tissue," Proc. SPIE **11113**, 111130N (2019).

35. M. Töpperwien, F. van der Meer, C. Stadelmann, and T. Salditt, "Correlative x-ray phase-contrast tomography and histology of human brain tissue affected by alzheimer's disease," NeuroImage **210**, 116523 (2020).

36. M. Banich, "Interhemispheric interaction: mechanisms of unified processing," in *Hemispheric Communication: Mechanisms and Models*, F. Kitterle, ed. (Routledge, 1995), pp. 271–300.

37. A. Siegel and H. N. Sapru, *Essential Neuroscience* (Lippincott Williams & Wilkins, 2006).

38. E. Jurrus, M. Hardy, T. Tasdizen, P. T. Fletcher, P. Koshevoy, C.-B. Chien, W. Denk, and R. Whitaker, "Axon tracking in serial block-face scanning electron microscopy," Med. Image Anal. **13**(1), 180–188 (2009).

39. W. Denk and H. Horstmann, "Serial block-face scanning electron microscopy to reconstruct three-dimensional tissue nanostructure," PLoS Biol **2**(11), e329 (2004).

40. D. Smith and T. Starborg, "Serial block face scanning electron microscopy in cell biology: Applications and technology," Tissue and Cell **57**, 111–122 (2019).

41. A. Cedola, A. Bravin, I. Bukreeva, M. Fratini, A. Pacureanu, A. Mittone, L. Massimi, P. Cloetens, P. Coan, G. Campi, R. Spanó, F. Brun, V. Grigoryev, V. Petrosino, C. Venturi, M. Mastrogiacomo, N. K. d. Rosbo, and A. Uccelli, "X-ray phase contrast tomography reveals early vascular alterations and neuronal loss in a multiple sclerosis model," Sci. Rep. **7**(1), 5890 (2017).

42. A. T. Kuan, J. S. Phelps, L. A. Thomas, T. M. Nguyen, J. Han, C.-L. Chen, A. W. Azevedo, J. C. Tuthill, J. Funke, P. Cloetens, A. Pacureanu, and W.-C. A. Lee, "Dense neuronal reconstruction through x-ray holographic nano-tomography," Nat. Neurosci. **23**(12), 1637–1643 (2020).

43. R. H. Masland, "Neuronal cell types," Curr. Biol. **14**(13), R497–R500 (2004).

44. C. Stadelmann, M. Albert, C. Wegner, and W. Brück, "Cortical pathology in multiple sclerosis," Curr. Opin. Neurol. **21**(3), 229–234 (2008).

45. J. Silver and J. H. Miller, "Regeneration beyond the glial scar," Nat. Rev. Neurosci. **5**(2), 146–156 (2004).

46. M. V. Sofroniew and H. V. Vinters, "Astrocytes: biology and pathology," Acta Neuropathol. **119**(1), 7–35 (2010).

47. W. Brück and C. Stadelmann, "Inflammation and degeneration in multiple sclerosis," Neurol. Sci. **24**(0), s265–s267 (2003).

48. A. Kutzelnigg, C. F. Lucchinetti, C. Stadelmann, W. Brück, H. Rauschka, M. Bergmann, M. Schmidbauer, J. E. Parisi, and H. Lassmann, "Cortical demyelination and diffuse white matter injury in multiple sclerosis," Brain **128**(11), 2705–2712 (2005).

49. M. Filippi, W. Brück, D. Chard, F. Fazekas, J. J. Geurts, C. Enzinger, S. Hametner, T. Kuhlmann, P. Preziosa, À. Rovira, K. Schmierer, C. Stadelmann, and M. A. Rocca, "Association between pathological and mri findings in multiple sclerosis," The Lancet Neurol. **18**(2), 198–210 (2019).

50. P. Patrikios, C. Stadelmann, A. Kutzelnigg, H. Rauschka, M. Schmidbauer, H. Laursen, P. S. Sorensen, W. Brück, C. Lucchinetti, and H. Lassmann, "Remyelination is extensive in a subset of multiple sclerosis patients," Brain **129**(12), 3165–3172 (2006).

51. E. Eggl, S. Schleede, M. Bech, K. Achterhold, R. Loewen, R. D. Ruth, and F. Pfeiffer, "X-ray phase-contrast tomography with a compact laser-driven synchrotron source," Proc. Natl. Acad. Sci. **112**(18), 5567–5572 (2015).

52. T. Salditt, M. Osterhoff, M. Krenkel, R. N. Wilke, M. Priebe, M. Bartels, S. Kalbfleisch, and M. Sprung, "Compound focusing mirror and x-ray waveguide optics for coherent imaging and nano-diffraction," J. Synchrotron Radiat. **22**(4), 867–878 (2015).

53. J. Soltau, M. Vassholz, M. Osterhoff, and T. Salditt, "Inline holography with hard x-rays at sub-15 nm resolution," Optica **8**(6), 818–823 (2021).

54. M. Stampanoni, R. Mokso, F. Marone, J. Vila-Comamala, S. Gorelick, P. Trtik, K. Jefimovs, and C. David, "Phase-contrast tomography at the nanoscale using hard x rays," Phys. Rev. B **81**(14), 140105 (2010).

55. J. C. da Silva, A. Pacureanu, Y. Yang, F. Fus, M. Hubert, J. Bloch, M. Salome, S. Bohic, and P. Cloetens, "High-energy cryo x-ray nano-imaging at the id16a beamline of esrf," Proc. SPIE **10389**, 103890F (2017).

56. J. C. Da Silva, A. Pacureanu, Y. Yang, S. Bohic, C. Morawe, R. Barrett, and P. Cloetens, "Efficient concentration of high-energy x-rays for diffraction-limited imaging resolution," Optica **4**(5), 492–495 (2017).

57. H. D. King, "The effects of formaldehyde on the brain," J. Comp. Neurol. **23**(4), 283–314 (1913).

58. M. Brown, R. Reed, and R. Henry, "Effects of dehydration mediums and temperature on total dehydration time and tissue shrinkage," J. Plast. **17**, 28–33 (2002).

59. J. Buytaert, J. Goyens, D. De Greef, P. Aerts, and J. Dirckx, "Volume shrinkage of bone, brain and muscle tissue in sample preparation for micro-ct and light sheet fluorescence microscopy (lsfm)," Microsc. Microanal. **20**(4), 1208–1217 (2014).

60. D. G. Robinson, U. Ehlers, R. Herken, B. Herrmann, F. Mayer, and F.-W. Schürmann, *Methods of Preparation for Electron Microscopy* (Springer Berlin Heidelberg, 1987).

61. M. C. Willingham and A. V. Rutherford, "The use of osmium-thiocarbohydrazide-osmium (OTO) and ferrocyanide-reduced osmium methods to enhance membrane contrast and preservation in cultured cells," J. Histochem. Cytochem. **32**(4), 455–460 (1984).

62. L. B. Dahlin, K. R. Rix, V. A. Dahl, A. B. Dahl, J. N. Jensen, P. Cloetens, A. Pacureanu, S. Mohseni, N. O. Thomsen, and M. Bech, "Three-dimensional architecture of human diabetic peripheral nerves revealed by x-ray phase contrast holographic nanotomography," Sci. Rep. **10**(1), 7592 (2020).

63. M.-T. Weil, S. Heibeck, M. Töpperwien, S. tom Dieck, T. Ruhwedel, T. Salditt, M. C. Rodicio, J. R. Morgan, K.-A. Nave, W. Möbius, and H. B. Werner, "Axonal ensheathment in the nervous system of lamprey: implications for the evolution of myelinating glia," J. Neurosci. **38**(29), 6586–6596 (2018).

64. P. Parlanti, V. Cappello, F. Brun, G. Tromba, R. Rigolio, I. Tonazzini, M. Cecchini, V. Piazza, and M. Gemmi, "Size and specimen-dependent strategy for x-ray micro-ct and tem correlative analysis of nervous system samples," Sci. Rep. **7**(1), 2858 (2017).

65. L. Massimi, I. Bukreeva, G. Santamaria, M. Fratini, A. Corbelli, F. Brun, S. Fumagalli, L. Maugeri, A. Pacureanu, P. Cloetens, N. Pieroni, F. Fiordaliso, G. Forloni, A. Uccelli, N. Kerlero de Rosbo, C. Balducci, and A. Cedola, "Exploring alzheimer's disease mouse brain through x-ray phase contrast tomography: From the cell to the organ," NeuroImage **184**, 490–495 (2019).

66. C. Bosch, T. Ackels, A. Pacureanu, Y. Zhang, C. J. Peddie, M. Berning, N. Rzepka, M.-C. Zdora, I. Whiteley, M. Storm, A. Bonnin, C. Rau, T. Margrie, L. Collinson, and A. T. Schaefer, "Functional and multiscale 3d structural investigation of brain tissue through correlative in vivo physiology, synchrotron micro-tomography and volume electron microscopy," bioRxiv (2021).

67. M. Busse, M. Müller, M. A. Kimm, S. Ferstl, S. Allner, K. Achterhold, J. Herzen, and F. Pfeiffer, "Three-dimensional virtual histology enabled through cytoplasm-specific x-ray stain for microscopic and nanoscopic computed tomography," Proc. Natl. Acad. Sci. **115**(10), 2293–2298 (2018).

68. M. Müller, M. A. Kimm, S. Ferstl, S. Allner, K. Achterhold, J. Herzen, F. Pfeiffer, and M. Busse, "Nucleus-specific x-ray stain for 3d virtual histology," Sci. Rep. **8**(1), 17855 (2018).

69. G. E. Sosinsky, J. Crum, Y. Z. Jones, J. Lanman, B. Smarr, M. Terada, M. E. Martone, T. J. Deerinck, J. E. Johnson, and M. H. Ellisman, "The combination of chemical fixation procedures with high pressure freezing and freeze

substitution preserves highly labile tissue ultrastructure for electron tomography applications," J. Struct. Biol. **161**(3), 359–371 (2008).

70. A. Robisch, J. Frohn, and T. Salditt, "Iterative micro-tomography of biopsy samples from truncated projections with quantitative gray values," Phys. Med. Biol. **65**(23), 235034 (2020).